Thickness-Dependent Crossover from Charge- to Strain-Mediated Magnetoelectric Coupling in Ferromagnetic/Piezoelectric Oxide Heterostructures

Steven R. Spurgeon,[†] Jennifer D. Sloppy,[†] Despoina Maria (Demie) Kepaptsoglou,[‡] Prasanna V. Balachandran,[†] Siamak Nejati,[§,□] J. Karthik,[⊥] Anoop R. Damodaran,[⊥] Craig L. Johnson,[∥] Hailemariam Ambaye,[#] Richard Goyette,[#] Valeria Lauter,[#] Quentin M. Ramasse,[‡] Juan Carlos Idrobo,[△] Kenneth K. S. Lau,[§] Samuel E. Lofland, Jr.,[▽] James M. Rondinelli,[†] Lane W. Martin,[⊥] and Mitra L. Taheri[†,*]

[†]Department of Materials Science and Engineering, Drexel University, Philadelphia, Pennsylvania, United States, [‡]SuperSTEM, STFC Daresbury Laboratories, Warrington, United Kingdom, [§]Department of Chemical and Biological Engineering, Drexel University, Philadelphia, Pennsylvania, United States, [⊥]Department of Materials Science and Engineering/Materials Research Laboratory, University of Illinois, Urbana—Champaign, Urbana, Illinois, United States, [∥]Centralized Research Facilities, College of Engineering, Drexel University, Philadelphia, Pennsylvania, United States, [#]Neutron Sciences Directorate, Oak Ridge National Laboratory, Oak Ridge, Tennessee, United States, [△]Center for Nanophase Materials Sciences Division, Oak Ridge National Laboratory, Oak Ridge, Tennessee, United States, and [▽]Department of Physics and Astronomy, Rowan University, Glassboro, New Jersey, United States. [□]Present address: Department of Chemical and Environmental Engineering, Yale University, New Haven, Connecticut, United States.

ABSTRACT Magnetoelectric oxide heterostructures are proposed active layers for spintronic memory and logic devices, where information is conveyed through spin transport in the solid state. Incomplete theories of the coupling between local strain, charge, and magnetic order have limited their deployment into new information and communication technologies. In this study, we report direct, local measurements of strain- and charge-mediated magnetization changes in the $La_{0.7}Sr_{0.3}MnO_3/PbZr_{0.2}Ti_{0.8}O_3$ system using spatially resolved characterization techniques in both real and reciprocal space. Polarized neutron reflectometry reveals a graded magnetization that results from both local structural distortions and interfacial screening of bound surface charge from the adjacent ferroelectric. Density functional theory calculations support the experimental observation that strain locally suppresses the magnetization through a change in the Mn-e_g orbital polarization. We suggest that this local coupling and magnetization suppression may be tuned by controlling the manganite and ferroelectric layer thicknesses, with direct implications for device applications.

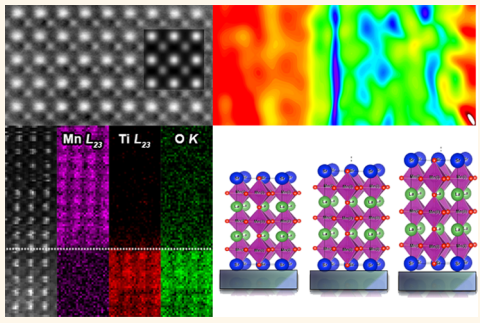

KEYWORDS: spintronics · magnetoelectrics · strain engineering · polarized neutron reflectometry · transmission electron microscopy

Over the past decade great strides have been made toward electronics that utilize both electron charge and spin.[1,2] For instance, spin-transfer torque memories rely on the injection of a spin-polarized current to flip the magnetization of a free layer in a magnetic tunnel junction.[3,4] Direct control of spin polarization would greatly optimize the performance of such devices, enabling more robust and efficient computing architectures by conveying information through spin transport in the solid state.[5−8] Recent advances in thin-film growth techniques have enabled the synthesis of oxide heterostructures where strain and charge effects are used to reversibly control spin polarization and magnetization at interfaces.[9−15] In particular there is growing interest in the connection between strain and magnetism in materials, most notably in the active tuning of magnetization *via* a coupling of local strain gradients and spin states through the so-called "flexomagnetic" effect.[16,17] Flexomagnetism

* Address correspondence to mtaheri@coe.drexel.edu.

Received for review October 29, 2013 and accepted December 7, 2013.

Published online December 08, 2013
10.1021/nn405636c

describes the interactions between strain gradients and local spins; the presence of varying local strains may therefore give rise to a sizable flexomagnetic contribution to magnetization.[16−18]

The current understanding of localized strain and charge-transfer effects on magnetization is limited, since previous studies have relied on nonlocal probes that are unable to directly map strain and valence changes.[19] Studies of magnetoelectric heterostructures of the ferromagnetic, half-metal $La_{1-x}Sr_xMnO_3$ (LSMO) and the piezoelectric $PbZr_xTi_{1-x}O_3$ (PZT) exemplify the inherent complexity of these systems. Previous work has found that charge-transfer screening of the adjacent ferroelectric layer is largely responsible for coupling in ultrathin (<4 nm) LSMO films on PZT,[20−22] while other studies have shown that variations in layer thickness and interfacial strain can also affect magnetization.[23−28] In these studies the local strain state of the LSMO/PZT interface was not measured. The relationship between interfacial strain and chemistry is also an important consideration in controlling the behavior of these materials, since previous studies have shown that strain fields around dislocations can act as fast paths for interfacial interdiffusion in LSMO/PZT.[29,30] It remains unclear how local strains evolve as a function of layer thickness, how strain and charge-transfer screening act in concert to mediate interfacial magnetization, and, more importantly, how to deterministically control this behavior.

To better understand flexomagnetism and magnetoelectric coupling in oxides, it is necessary to move beyond bulk probes of strain and magnetization toward local measurements of strain and interfacial charge-transfer screening.[31−33] Here we synthesize heterostructures with different local strain and polarization states. Using a combination of local atomic and magnetic characterization, in conjunction with density functional theory (DFT) calculations, we find evidence for significant strain-induced magnetization changes. We show that large strain changes occur throughout the magnetic layer and that they can be tuned by an appropriate choice of substrate thickness. Furthermore, we show evidence for interfacial charge-transfer screening, which is secondary to dominant strain effects in thicker layers. Our analysis suggests that it is possible to favor a particular coupling mode by an appropriate choice of ferromagnet and ferroelectric layer thickness. By using local probes of structure and magnetization we are able to resolve strain and magnetization changes within each layer that would be inseparable by bulk techniques.

RESULTS AND DISCUSSION

We used a substrate-induced self-poling technique to vary the electrostatic boundary conditions of the bottom electrode interface, so as to pole the PZT away from (on $La_{0.7}Sr_{0.3}MnO_3$ (LSMO)) or toward (on $SrRuO_3$ (SRO)) the substrate, which we term as poled-up and -down, respectively.[34−38] Using this method it is possible to control the polarization of the PZT without the need for large, leaky planar electrodes that would preclude neutron measurements. Four heterostructures were deposited on single-crystal $SrTiO_3$ (001) substrates by pulsed laser deposition (PLD). Oxide metal underlayers of either LSMO or SRO were deposited on a bulk $SrTiO_3$ substrate, followed by either a "thick" (23−37 nm) or "thin" (13 nm) $PbZr_{0.2}Ti_{0.8}O_3$ layer and a cap of ∼10−19 nm LSMO, as shown in Figure 1. These thicknesses were chosen to explore the changes in strain profiles associated with gradual relaxation of PZT to the bulk.

Aberration-corrected scanning transmission electron microscopy (STEM) was conducted to confirm the quality of the LSMO/PZT interfaces. High-angle annular dark field (HAADF) images show that the layer thicknesses are nominally constant in the plane of the film (Figure 1 and Supporting Information). The reversal of the PZT polarization between the LSMO and SRO underlayers is also confirmed locally by measuring the Ti^{4+} cation displacement at several points along the interface (Figure 1C,G).[39] Since all the film layers were grown *in situ*, it was not possible to conduct piezoresponse force microscopy (PFM) measurements without disturbing the pristine interfaces between each layer. X-ray diffraction (XRD) shows that, in-plane, the films are constrained to the substrate (see Supporting Information). However, as we later discuss, the local strain state of the top LSMO layer varies greatly depending on the choice of underlayer and PZT thickness.

Macroscopic magnetic hysteresis measurements (Figure 2A,B) reveal a thickness-dependent saturation magnetization (M_S). The data shown have been normalized to the entire thickness of LSMO present in each sample. A remarkable 50% (∼0.6 μ_B/Mn) difference in M_S occurs between poled-up and -down heterostructures based on thick PZT (Figure 2A). A smaller 10−20% (0.1−0.2 μ_B/Mn) difference in M_S occurs between poled-up and -down heterostructures based on thin PZT (Figure 2B). For comparison, $M_S \approx 1$ μ_B/Mn is expected for $La_{0.67}Sr_{0.3}MnO_3$ at room temperature.[40] These differences are also reflected in the Curie temperature (T_C) (Figure 2C): the samples deposited on the thin PZT have a T_C of 335−342 K, while the samples on thick PZT show a T_C of 328−331 K, compared to a nominal bulk T_C of ∼360 K.[41]

To probe the local origin of these magnetization differences, polarized neutron reflectometry (PNR) was conducted at 298 K with an in-plane magnetic field of 1 T. Magnetization depth profiles (Figure 2D−G) show that the M_S of the top LSMO layer varies spatially but is generally suppressed near the vacuum surface as well as at the PZT interface, as has been previously observed.[42] Strain-induced distortions of LSMO can

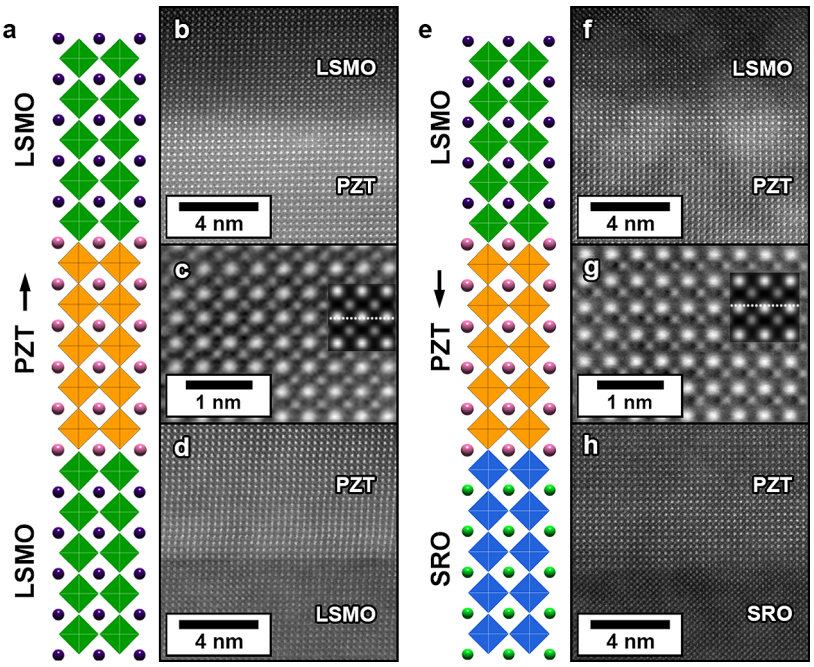

Figure 1. (A, E) Illustration of the two film structures used in this study, with the PZT polarization direction indicated by the arrows. Characteristic high-angle annular dark field (STEM-HAADF) images of the top (B, F) and bottom (D, H) PZT interfaces, showing the absence of any extrinsic defects. (C, G) Cross-correlated images of the PZT layer, confirming the change in polarization; the insets are the result of multislice simulations, with the horizontal dash corresponding to the center of the unit cell.

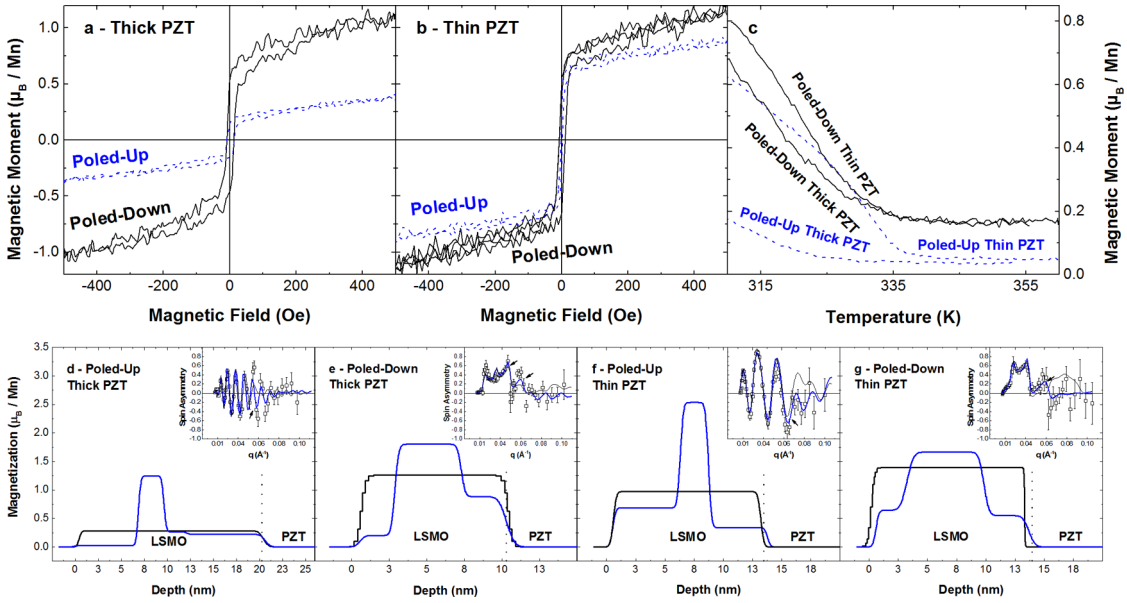

Figure 2. Top: (A, B) In-plane vibrating sample magnetometry (VSM) measurements conducted at 305 K along the [100] substrate direction, showing a ~50% increase in saturation between the poled-up and poled-down thick PZT samples (A) and a 10–20% increase in saturation for the thin PZT samples (B). (C) Moment *versus* temperature measurements conducted in a 100 Oe magnetic field measured on heating show a significant enhancement of T_C with decreasing PZT thickness. Bottom: (D–G) Polarized neutron reflectometry (PNR) magnetization depth profiles measured at 298 K and with an in-plane magnetic field of 1 T along the [100] substrate direction. The insets show the measured spin asymmetry $(R^{++} - R^{--})/(R^{++} + R^{--})$ and the fits to the data. The vertical dashed lines mark the boundaries between adjacent film layers. The lighter (black) lines are a model that assumes uniform magnetization throughout each LSMO layer, while the heavier (blue) lines are a model that allows for graded magnetization through the LSMO. The arrows in the inset show regions of improved fitting (as indicated by a smaller chi-squared value). There is a clear suppression of magnetization across the majority of the top LSMO layer in D, as well as suppression near the vacuum and PZT interfaces in the other samples E–G.

suppress T_C and consequently room-temperature magnetization.[43–46] The suppression of T_C due to strain-induced distortions in LSMO results from changes in the Mn–O–Mn bond angles that govern electron hopping between the Mn-e_g states responsible for double exchange.[47–49] Because of the sensitivity of

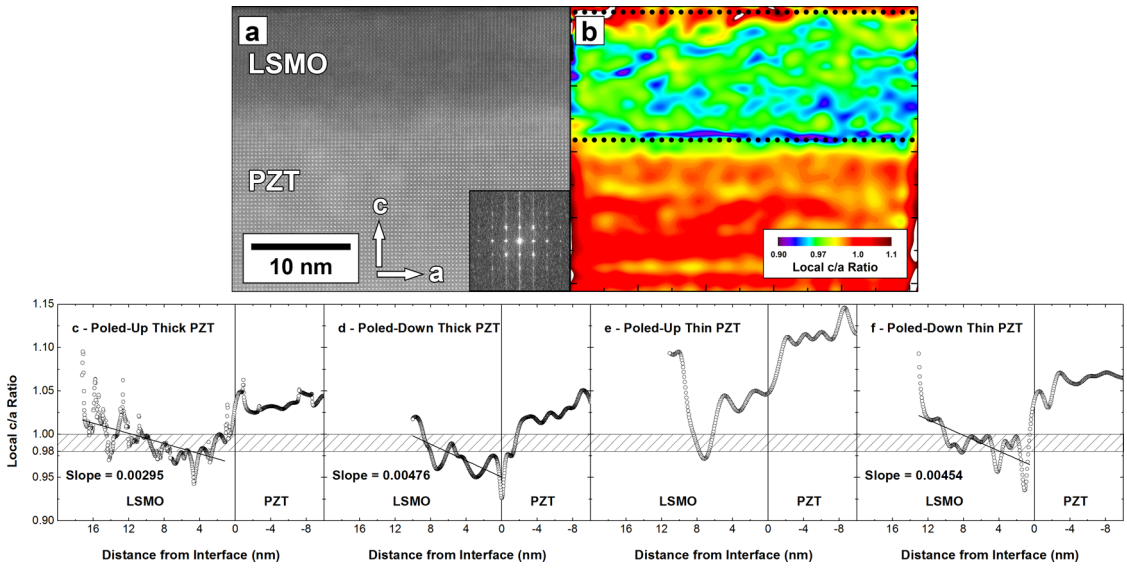

Figure 3. (A) Characteristic STEM-HAADF micrograph of the LSMO/PZT interface; the inset shows the fast Fourier transform of the PZT layer. (B) Characteristic map of local *c*/*a* axial ratios in the LSMO and PZT layers. This ratio varies throughout the LSMO but is largest at the vacuum interface. (C−F) Line scans of *c*/*a* normal to the LSMO/PZT interface for all four films. The vertical line indicates the PZT boundary, while the horizontal dashed region indicates the *c*/*a* range outside of which magnetization is expected to be suppressed.

the double-exchange mechanism to strain, local strain fluctuations—if present—may give rise to the graded magnetization profiles observed in PNR.

Geometric phase analysis (GPA) was used to test this hypothesis by measuring strains directly from TEM micrographs with ∼0.1% accuracy down to the nanometer scale.[50,51] In all samples the in-plane strain is essentially uniform over the 3−5 nm integration window, varying by <0.1%. We note that there is good agreement between the average GPA-measured *c*/*a* axial ratios and those measured by XRD (see supplemental Table SII). The out-of-plane strain relative to bulk unstrained LSMO increases normal to the PZT interface, reaching a maximum at the vacuum surface. Using this technique we are able to map the local *c*/*a* axial ratio within each sample (Figure 3B). This analysis reveals that for both thick PZT samples (Figure 3C,D) the *c*/*a* of the LSMO increases from ∼0.96 at the PZT interface to 1.01−1.03 at the vacuum surface. This corresponds to a strain gradient of approximately (2.95−4.76) × 10^6 m^{-1}. The poled-down thin PZT sample (Figure 3F) shows a similar trend, increasing from ∼0.98 at the PZT interface to ∼1.03 at the vacuum surface (a gradient of 4.76 × 10^6 m^{-1}). However, the poled-up thin PZT sample (Figure 3E) shows a U-shaped profile that drops from ∼1.04 at the PZT interface to ∼0.97 at the middle of the LSMO and increases to ∼1.05 at the vacuum surface. The changes coincide with significantly different *c*/*a* ratios in the adjacent PZT layer, which ranges from 1.04 to 1.1, suggesting that the interfacial strain state is heavily dependent on the tetragonality of the underlying PZT layer, as well as the thickness of the LSMO layer. More importantly, a comparison of the PNR and GPA data shows that, in general, an LSMO *c*/*a* that deviates outside of the range 0.98−0.995 coincides with local suppression of magnetization, which agrees well with changes in bulk properties.[52] The observed strain fluctuations may correlate to local spin changes, particularly since they are comparable in magnitude to the strains needed to induce a measurable flexoelectric effect in other systems.[53,54] While direct flexomagnetism is limited to a subset of symmetry classes, indirect flexomagnetism is expected to be present in all magnetoelectrics, wherever polarization and magnetization are coupled.[55]

To estimate the strain-induced suppression of magnetization in the samples, we turn to the empirical model of Millis *et al.*[47] and density functional theory (DFT) calculations. Millis *et al.* proposed a model that relates T_C to the substrate strain-induced enhancement of the Jahn−Teller distortion relative to unstrained bulk LSMO (see Experimental Section).[47,56] We choose this model since it allows us to directly substitute the averaged local $\langle c/a \rangle$, extracted from the experimental GPA, to obtain an estimate of T_C. We then conducted DFT calculations to explore the electron−lattice effects mediating the microscopic coupling in detail.

For the poled-up PZT samples we find from GPA that $\langle c/a \rangle_{LSMO} \approx 0.99-1.01$, and we estimate $T_C \approx 249-295$ K for the top LSMO layer using the Millis *et al.* model. These out-of-plane strains appear to greatly suppress the ferromagnetic ordering of the top layer, as is observed in PNR (Figure 2D,F). In contrast, for the poled-down samples, we find that $\langle c/a \rangle_{LSMO} \approx 0.98-0.995$, and we estimate $T_C \approx 319-327$ K. These distortions result in a higher T_C and larger average

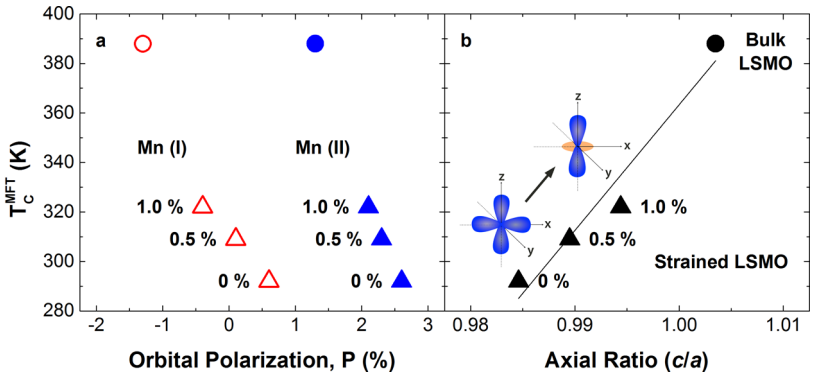

Figure 4. (A) Relationship between T_C^{MFT} (K) and P (in %) for various simulation cells as calculated from DFT. Positive value for P indicates the percentage excess of Mn-e_g electrons filling the $d_{x^2-y^2}$ orbital relative to the d_{z^2} orbital and *vice versa*. The 30-atom supercell contains two distinct Mn atoms, Mn(I) (open, red) and Mn(II) (filled, blue) (see Supporting Information). (B) Relationship between T_C^{MFT} (K) and axial ratio (c/a) as calculated from DFT. A clear trend emerges between c/a, P, and T_C^{MFT}. In unstrained LSMO, both $d_{x^2-y^2}$ and d_{z^2} are filled. The application of in-plane tensile strain promotes preferential $d_{x^2-y^2}$ filling in both Mn atoms; simultaneously T_C^{MFT} decreases. However, out-of-plane stretching gradually promotes transfer of charge to d_{z^2} orbitals, and a corresponding gradual increase in T_C^{MFT} is found. Circles correspond to bulk LSMO, and triangles are epitaxially strained LSMO (under uniaxial strain varying from 0 to 1% along the [001] direction).

magnetization across the LSMO (Figure 2E,G). The predicted and measured Curie temperatures for the poled-down samples are in excellent agreement (Figure 2C); however, the agreement for the poled-up samples is worse, perhaps because these samples include two LSMO layers and the measurement of T_C is less accurate.

We next perform spin-polarized DFT calculations within the generalized-gradient approximation plus Hubbard-U method on a series of LSMO structures to isolate the contributions of epitaxial strain from interfacial charge transfer on T_C and Mn-e_g orbital polarization. We choose lattice constants consistent with the experimental epitaxial constraints and $\langle c/a \rangle_{LSMO}$ ratios ranging from 0.985 (poled-up thick PZT) to 0.994 (poled-down thick PZT). We note that these axial ratios refer to the metric shape of the simulation cell, not local octahedral elongations, and thus deviations from the local strain measurements determined using GPA are expected. The atomic positions are then fully relaxed, allowing for rotations and bond elongations. First we computed the optimal $\langle c/a \rangle$ for LSMO on (001)-oriented STO and obtained a value of 0.985, which is consistent with the average $\langle c/a \rangle$ of LSMO on poled-up thick PZT. We then applied 0.5% and 1% uniaxial strain along the [001] direction to simulate the range of observed axial ratios (Figure 4), as a means to disentangle the strain contributions from interface effects due to coherent strain of LSMO with varying PZT thickness and polarization. We then calculated a mean-field theoretical ferromagnetic Curie temperature, T_C^{MFT}, following the procedure in Kübler *et al.*[57] and Lampis *et al.*[58]

Our DFT results indicate that out-of-plane stretching monotonically increases T_C^{MFT} from 292 K (0%) to 323 K (1%) at the highest $\langle c/a \rangle$ state. Our T_C^{MFT} trend compares favorably with our measured poled-up PZT samples that have LSMO underlayers as well as the model calculations following Millis *et al.* To quantify the orbital occupancy, we calculated the electron orbital polarization, $P = (n_{x^2-y^2} - n_{z^2})/n_{x^2-y^2} + n_{z^2})$, of Mn-$e_g$ orbitals from the partial density of states (PDOS) spectra, where $n_{x^2-y^2}$ and n_{z^2} are the area under the curve for $d_{x^2-y^2}$ and d_{z^2} orbitals, respectively, integrated up to the Fermi level.[59] A positive value for P indicates that electrons favor $d_{x^2-y^2}$ orbital occupancy, and a negative P value indicates that electrons favor d_{z^2} occupancy. We find that in bulk unstrained LSMO P takes both negative and positive values, and the magnitude of P is roughly the same for both Mn sites (Figure 4 and Figure S9); T_C^{MFT} for bulk LSMO is estimated to be 388 K. Application of an in-plane tensile strain alone promotes preferential $d_{x^2-y^2}$ orbital filling; P takes only positive values at both Mn sites, and T_C^{MFT} reduces drastically to 292 K, which agrees well with our experimental measurements made on poled-up samples. Uniaxial strain along [001] gradually transfers charge to the Mn d_{z^2} orbital aligned along the z-direction, as expected.[44,60,61] At 1% elongation, P becomes both negative and positive ($T_C^{MFT} \approx 322$ K), albeit reduced relative to unstrained LSMO. Commensurate with the filling of d_{z^2} orbitals as a function of out-of-plane stretching, T_C^{MFT} is also found to increase, indicating a direct association between the c/a axial ratio, macroscopic T_C^{MFT}, and P in LSMO.

Although a clear trend emerges between c/a, T_C, and P, in agreement with previous literature,[62,63] we recognize that our DFT calculations do not fully capture the T_C behavior of the poled-up samples. While these samples have the largest average $\langle c/a \rangle$ value (as measured by XRD), their measured T_C is lower than that of other samples, indicating the existence of an additional competing mechanism not captured in our simulations. We also note that these calculations are done

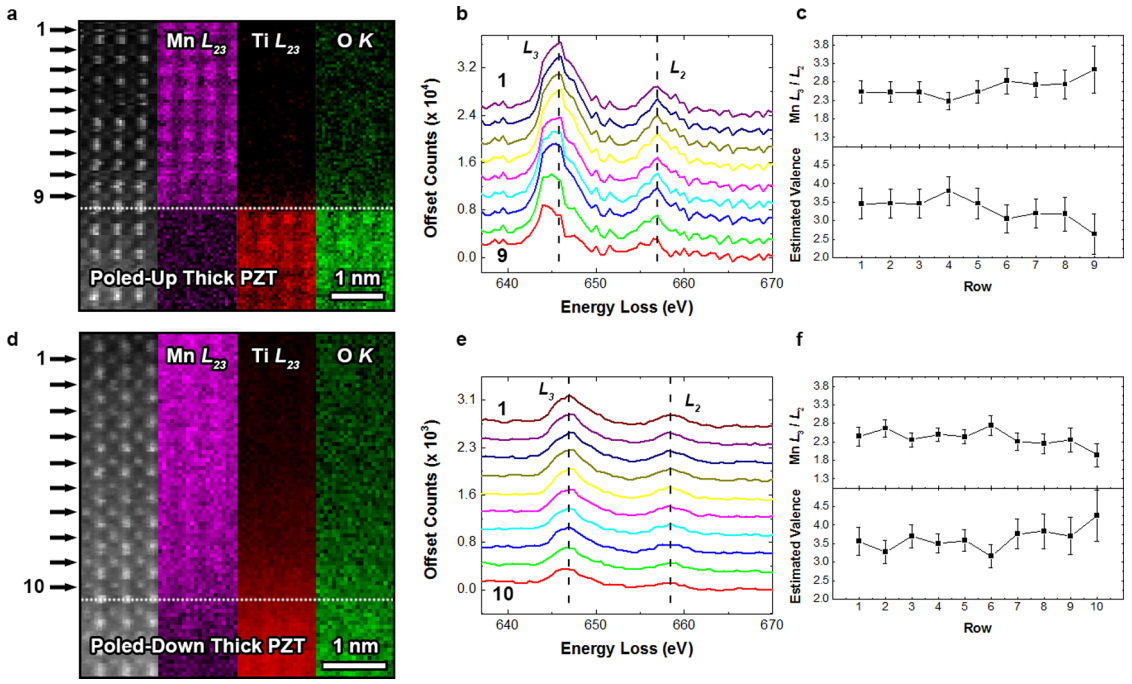

Figure 5. High-angle annular dark field images and electron energy loss spectroscopy maps of the top LSMO/PZT interface in the poled-up (A) and poled-down (D) thick PZT samples. The numbers indicate the atomic rows across which average spectra were collected and correspond to the Mn L_{23} spectra in B and E. (C, F) Calculated Mn L_3/L_2 ratios and estimated Mn valences from each row. Error bars correspond to the standard error of the Gaussian fits to the edges. Although both samples possess the same valence in the bulk (~3.4), they diverge near the PZT interface, indicating screening of surface charge from the adjacent PZT layer.

assuming a uniform uniaxial strain, in contrast to the changing strain observed in GPA; nonetheless, we believe that these results provide a valuable insight into how increasing tetragonality affects electronic and magnetic ordering.

To probe other possible coupling mechanisms, such as chemistry changes or charge-transfer screening, we have conducted electron energy loss spectroscopy (EELS) mapping of the LSMO/PZT interface. The Mn L_{23} white lines near 640−665 eV are measured in this study since they contain information about excitations from the spin−orbit split $2p_{3/2}$ and $2p_{1/2}$ levels to available states in the 3d band.[64−69] Screening of surface charge from the adjacent PZT layer gives rise to a change in the local 3d band occupancy, reflected in a deviation from the nominal Mn^{3+}/Mn^{4+} ratio of ~3.3.[70,71]

Figure 5 shows the results of STEM-EELS maps at the LSMO/PZT interface for the thick samples. We find that the interfaces are quite sharp, with the EELS signal limited to one to two atomic planes away from the interface; however, because STEM is a localized technique, it is impossible to completely rule out some intermixing in either interface. Both samples possess a bulk valence of ~3.4 (near the nominal 3.3), but at the interface the value for the poled-up sample drops to ~2.63, while that of the poled-down sample increases to ~4.26. Additionally, there is a clear shift of the Mn L_3 edge toward lower energy in the poled-up sample (Figure 5B), indicating lower valence; however, the shift in the poled-down sample is not as pronounced.[68,70] The valence change is spread over 3−4 unit cells at the interface, with an average valence at ~3.02 for poled-down and ~3.89 for poled-up, a difference of ~0.87. It should be noted that the error bars on this data are still rather large, ruling out more detailed analysis of the induced valence, but there is clearly an interfacial change likely resulting from interaction with the adjacent ferroelectric layer.

Thus, while local strain fluctuations suppress magnetization across larger length scales, it appears that charge-transfer screening operates in a ~2 nm interface region at the PZT boundary (Figure 2D−G), in line with prior estimates.[72−74] PNR measurements show that the change between states in the thick samples at 298 K is $\Delta m = m_{down} - m_{up} = 0.88 - 0.22 = 0.66\ \mu_B$/Mn, while, for the thin samples, $\Delta m = 0.54 - 0.34 = 0.20\ \mu_B$/Mn. These values agree well with previous magneto-optical studies of ultrathin LSMO that found $\Delta m = 0.76\ \mu_B$/Mn.[20]

CONCLUSIONS

Several trends are now clear. We find that it is possible to self-pole PZT through the use of an appropriate substrate material, a method that may be extended to many other systems. Macroscopic bulk magnetization measurements show that M_S and T_C depend on both PZT polarization and thickness. PNR measurements reveal that M_S varies locally and is most suppressed

at the LSMO/vacuum interface, where the GPA-measured LSMO *c*/*a* axial ratio is largest. Furthermore, we find evidence for large strain gradients ($\sim 10^6$ m^{-1}) in the LSMO. Phenomenological models show that local strains affect the Mn-e_g electronic distribution and play a role in suppressing the LSMO T_C. EELS and PNR also reveal the presence of a ~2 nm charge-transfer screening region that affects magnetization at the PZT interface. However, the magnitude of the induced magnetization does not directly agree with the previous work of Vaz *et al.*, suggesting that other factors may be at work.[20]

Collectively the results obtained in this study suggest a more complex model of strain- and charge-mediated magnetization in ferroelectric/ferromagnet composites. We find that the tetragonality of the PZT has a pronounced effect on the interfacial strain in the LSMO: a larger PZT *c*/*a* corresponds to a larger interfacial *c*/*a* in the LSMO, which gradually increases near the vacuum surface. In the ultrathin limit (<4 nm), strain fluctuations in LSMO are minimal and charge-transfer screening drives coupling. As the LSMO thickness increases, local strain fluctuations soon overwhelm the magnetization of the layer, indicating that layer geometries are crucial components in the design of these materials. In excess of the ultrathin limit, our PNR results indicate that local strain can induce much larger changes in the magnetization profile of LSMO than charge-transfer screening. By tuning the PZT tetragonality through doping or an appropriate substrate, it is possible to reshape magnetization gradients in the ferromagnet. Our results suggest that a piezoelectric substrate may be used to actively control local strain and directly vary the spin state of the ferromagnet. The wealth of insight provided by this suite of techniques shows that local probes of magnetization, strain, and chemistry are an invaluable way to understand coupling of multiple degrees of freedom in magnetoelectrics and emerging flexomagnets.

EXPERIMENTAL SECTION

$SrRuO_3$ and $PbZr_{0.2}Ti_{0.8}O_3$ films were grown by PLD at 635 °C at 100 and 200 mTorr pO_2, with laser repetition rates of 12 and 3 Hz and laser fluences of 1.75 and 2 J cm^{-2}, respectively. The $La_{0.7}Sr_{0.3}MnO_3$ layers were grown at 650 °C at 200 mTorr of oxygen with a laser repetition rate of 2 Hz and a fluence of 1.5 J cm^{-2}. Films were then cooled to room temperature in 760 Torr pO_2.

The crystallinity of the as-grown films was measured by XRD with Cu Kα radiation (λ = 0.15418 nm) on a Panalytical Empyrean diffractometer. Reciprocal space maps were made around the STO 103 diffraction condition. Layer thickness was studied by X-ray reflectivity as measured on a Rigaku SmartLab diffractometer.

Bulk magnetometry was conducted with a Quantum Design vibrating sample magnetometer at 305 K along the [100] and [110] in-plane substrate directions, with no discernible difference in hysteresis. T_C was measured in the range 310−350 K under an applied in-plane magnetic field of 100 Oe. An Arrott−Belov analysis was conducted to determine T_C, assuming self-consistent samples (see Supporting Information).

PNR was conducted at 298 K with an in-plane magnetic field of 1 T applied along the [100] substrate direction. Non-spin-flip specular reflectivites were measured from q = 0.005 to 0.1 Å^{-1}. The reflectivity data were then fit with the ReflPak software package and refined in conjunction with XRD. A fit was conducted with uniform magnetization in the LSMO layers, and a second fit was conducted in which the magnetization was allowed to vary. The latter resulted in a better fit to the measured spin asymmetry, particularly at higher q.

Samples were prepared for TEM by conventional mechanical polishing and ion milling. HRTEM images were captured at 200 keV on a JEOL 2100 LaB_6. BF-STEM and STEM-HAADF micrographs were also captured on a C_S-corrected FEI Titan STEM operating at 300 keV. EELS maps and HAADF images were measured on a C_S-corrected Nion UltraSTEM 100 operating at 100 keV, with a convergence angle of 30 mrad and an effective energy resolution of 0.6−0.7 eV.[75] The background was removed from each scan using a power law fit, and spectra were extracted from each map row-by-row with a $\sim 0.1 \times 0.8 - 1$ nm^2 window. Hartree-Slater cross sections were subtracted from each edge, and the spectra were processed with the EELSTools package in Digital Micrograph to extract Mn L_{23} ratios from the positive component of the second derivative.[76]

Cation displacements were determined from a series of 10−40 STEM-HAADF acquisitions, which were captured at 5 μs intervals and cross-correlated and averaged with the ImageJ program with the StackReg plugin. Image simulations along the PZT [100] direction were conducted with the multislice method in the QSTEM program.[77] This allows us to achieve a precision to measure the atomic displacements better than ~8 pm.[78] Several atomic displacements were modeled with a 69 × 70 × 160 supercell consisting of 80 slices. A 400 × 400 pixel array with a 0.05 Å × 0.05 Å resolution and 20 Å × 20 Å window size was used, along with the microscope parameters.

GPA was conducted on STEM-HAADF and HRTEM images displaying minimal drift or scan error. First maps of local reciprocal lattice vectors corresponding to out-of-plane (g_1) and in-plane (g_2) directions were constructed. The ratio of these two maps (g_2/g_1) then gives the local *c*/*a*.[79] The line profiles shown in Figure 4 were measured by integrating 3−5 nm in-plane to minimize noise. It should be noted that local contrast and thickness fluctuations can give rise to local spikes in the measured ratio, so we only discuss broader trends in *c*/*a*.

To calculate in- (ε_{xx}) and out-of-plane (ε_{yy}) LSMO strains, references were chosen in either the STO or PZT layers; in the latter the measured strain values have been shifted to account for the average strain across the PZT layer. The measured strains in the top LSMO layer were converted relative to bulk LSMO according to

$$\varepsilon_{\text{relative}} = \left(\varepsilon_{\text{measured}} + \frac{c_{\text{STO, bulk}} - c_{\text{LSMO, bulk}}}{c_{\text{STO, bulk}}}\right)\frac{c_{\text{STO, bulk}}}{c_{\text{LSMO, bulk}}}$$

where $c_{\text{STO,bulk}}$ = 3.905 Å and $c_{\text{LSMO,bulk}}$ = 3.87 Å.

T_C was estimated from these GPA strains using the empirical model of Millis *et al.*[47]

$$T_C(\varepsilon) = T_C(\varepsilon = 0)\left(1 - \alpha\varepsilon_B - \frac{1}{2}\Delta\varepsilon_{JT}^2\right)$$

where $\varepsilon_B = (2\varepsilon_{xx} + \varepsilon_{yy})$ and $\varepsilon_{JT} = (2/3)^{1/2}(\varepsilon_{yy} - \varepsilon_{xx})$. $T_C(\varepsilon = 0)$ is the bulk LSMO T_C of ~360 K, while α and Δ are empirical constants that represent the weighting of the bulk strain and Jahn−Teller distortion of MnO_6 octahedra, respectively. Typical values are $\alpha \approx 10$ and $\Delta \approx 270$.[56]

DFT calculations were performed within the spin-polarized generalized gradient approximation (GGA) plus Hubbard-*U*

method as implemented in the Quantum-ESPRESSO package version 5.0.[80] The Dudarev *et al.* approach[80] was followed to include an effective Hubbard term of 3 eV for unstrained LSMO and 2 eV for LSMO on STO to accurately treat the correlated Mn 3d electrons. The core and valence electrons were treated with the ultrasoft pseudopotential[81] and the PBEsol exchange–correlation functional.[82,83] The Brillouin-zone integrations were performed with a Marzari–Vanderbilt smearing[84] of 0.02 Ry over a 7 × 7 × 5 Monkhorst–Pack *k*-point mesh[85] centered at Γ and a 60 and 600 Ry plane-wave and kinetic energy cutoff for charge density, respectively. For density of states (DOS) calculations, a denser 14 × 14 × 12 Monkhorst–Pack *k*-point mesh sampling was used. Atomic positions were allowed to converge until the Hellmann–Feynman forces became less than 2 meV Å^{-1}. Structure optimization was performed using the Broyden–Fletcher–Goldfarb–Shanno (BFGS) algorithm. The approach adapted by Ma *et al.*[86] was used to simulate the crystal structure of LSMO (see Supporting Information). Orbital polarization (*P*) was calculated using the formula

$$P = \frac{n_{x^2-y^2} - n_{z^2}}{n_{x^2-y^2} + n_{z^2}}$$

where $n_{x^2-y^2}$ and n_{z^2} are the area under the partial density of states spectra of $d_{x^2-y^2}$ and d_{z^2} orbitals respectively (for both spins) within the energy window from the Fermi level to −8 eV below it. The nearest-neighbor exchange coupling constant J_0 was calculated within the mean-field approximation[57,58] with

$$J_0 = \frac{E_F - E_{AFM-A}}{\frac{1}{2}\left(\sum S_1^F S_2^F - \sum S_1^{AFM-A} S_2^{AFM-A}\right)}$$

where E_F and E_{AFM-A} are the total energies (eV) of spin-polarized ferromagnetically ordered and spin polarized *A*-type antiferromagnetically ordered calculations, respectively, S_1 is the calculated atomic magnetic moment of the Mn(I) atom, and S_2 is the calculated atomic magnetic moment of the Mn(II) atom. From J_0, $\tilde{T}_C$ was estimated by the mean-field theory approximation, $\tilde{T}_C = (2/3)S(S+1)(J_0/k_B)$,[57,58] where $S = ((4S_1^F) + (2S_2^F))/6$ is the weighted average of the magnetic moments of Mn in the ferromagnetic spin order configuration.

Conflict of Interest: The authors declare no competing financial interest.

Acknowledgment. S.R.S. and M.L.T. thank Drs. Steven May and Rebecca Sichel-Tissot for constructive discussions. S.R.S. also thanks Christopher R. Winkler and Michael L. Jablonski for their assistance with TEM sample preparation. The authors gratefully acknowledge support from the National Science Foundation under grants CMMI-1031403 (M.L.T.), DMR-0908779 (S.E.L), DMR-0821406 (S.E.L.), CBET-0846245 (S.N. and K.K.S.L), and DMR-1149062 (J.K. and L.W.M.), as well as from the Office of Naval Research under grants N00014-1101-0296 (M.L.T.) and N00014-10-1-0525 (J.K. and L.W.M). A.R.D. and L.W.M. acknowledge support from the Army Research Office under grant W911NF-10-1-0482. P.V.B. and J.M.R. were supported by the Defense Advanced Research Projects Agency under grant N66001-12-4224. Electron microscopy and X-ray photoelectron spectroscopy (NSF MRI CBET-0959361) were conducted in Drexel University's Centralized Research Facilities, and X-ray reciprocal space mapping and magnetic measurements were performed in Rowan University's Department of Physics and Astronomy. X-ray diffraction work was also conducted in the Laboratory for Research on the Structure of Matter at the University of Pennsylvania. DFT modeling was conducted on the Cray XE6 Garnet system at the U.S. Army Engineer Research and Development Center. Part of this research was a user project supported by Oak Ridge National Laboratory's Center for Nanophase Materials Sciences (CNMS), which is sponsored by the Scientific User Facilities Division, Office of Basic Energy Sciences, U.S. Department of Energy (J.C.I.). Electron microscopy was carried out in part at SuperSTEM, the U.K. National Facility for Aberration-Corrected STEM supported by the U.K. Engineering and Physical Sciences Research Council. Polarized neutron reflectometry experiments were performed at the Spallation Neutron Source at Oak Ridge National Laboratory, managed by UT-Battelle, LLC, for the U.S. Department of Energy. Author S.R.S. is supported by a National Science Foundation Integrative Graduate Education and Research Traineeship (IGERT) and a Department of Defense National Defense Science and Engineering Graduate (NDSEG) Fellowship.

Supporting Information Available: Structural characterization and experimental details are available free of charge *via* the Internet at http://pubs.acs.org/.

REFERENCES AND NOTES

1. Bader, S.; Parkin, S. Spintronics. *Annu. Rev. Condens. Matter Phys.* **2010**, *1*, 71–88.
2. Fert, A. The Present and the Future of Spintronics. *Thin Solid Films* **2008**, *517*, 2–5.
3. Stiles, M.; Zangwill, A. Anatomy of Spin-Transfer Torque. *Phys. Rev. B* **2002**, *66*, 014407.
4. Sankey, J. C.; Cui, Y.-T.; Sun, J. Z.; Slonczewski, J. C.; Buhrman, R. A.; Ralph, D. C. Measurement of the Spin-Transfer-Torque Vector in Magnetic Tunnel Junctions. *Nat. Phys.* **2007**, *4*, 67–71.
5. Prinz, G. A. Magnetoelectronics. *Science* **1998**, *282*, 1660–1663.
6. Wolf, S.; Treger, D. Spintronics: A New Paradigm for Electronics for the New Millennium. *IEEE Trans. Magn.* **2000**, *36*, 2748–2751.
7. Fert, A.; George, J.-M.; Jaffrès, H.; Mattana, R.; Seneor, P. The New Era of Spintronics. *Europhys. News* **2003**, *34*, 227–229.
8. Wolf, S. A.; Awschalom, D. D.; Buhrman, R. A.; Daughton, J. M.; von Molnár, S.; Roukes, M. L.; Chtchelkanova, A. Y.; Treger, D. M. Spintronics: A Spin-Based Electronics Vision for the Future. *Science* **2001**, *294*, 1488–1495.
9. Eerenstein, W.; Wiora, M.; Prieto, J. L.; Scott, J. F.; Mathur, N. D. Giant Sharp and Persistent Converse Magnetoelectric Effects in Multiferroic Epitaxial Heterostructures. *Nat. Mater.* **2007**, *6*, 348–351.
10. Garcia, V.; Bibes, M.; Bocher, L.; Valencia, S.; Kronast, F.; Crassous, A.; Moya, X.; Enouz-Vedrenne, S.; Gloter, A.; Imhoff, D.; *et al.* Ferroelectric Control of Spin Polarization. *Science* **2010**, *327*, 1106–1110.
11. Thiele, C.; Dörr, K.; Schultz, L.; Beyreuther, E.; Lin, W.-M. Piezoelectrically Induced Resistance Modulations in $La_{0.7}Sr_{0.3}MnO_3$/Pb(Zr,Ti)O_3 Field Effect Devices. *Appl. Phys. Lett.* **2005**, *87*, 162512.
12. Martin, L.; Chu, Y.-H.; Ramesh, R. Advances in the Growth and Characterization of Magnetic, Ferroelectric, and Multiferroic Oxide Thin Films. *Mater. Sci. Eng., R* **2010**, *68*, 89–133.
13. Wang, Y.; Hu, J.; Lin, Y.; Nan, C.-W. Multiferroic Magnetoelectric Composite Nanostructures. *NPG Asia Mater.* **2010**, *2*, 61–68.
14. Bibes, M.; Barthélémy, A. Multiferroics: Towards a Magnetoelectric Memory. *Nat. Mater.* **2008**, *7*, 425–426.
15. Béa, H.; Gajek, M.; Bibes, M.; Barthélémy, A. Spintronics with Multiferroics. *J. Phys.: Condens. Matter* **2008**, *20*, 434221.
16. Lukashev, P.; Sabirianov, R. F. Flexomagnetic Effect in Frustrated Triangular Magnetic Structures. *Phys. Rev. B* **2010**, *82*, 094417.
17. Eliseev, E.; Morozovska, A.; Glinchuk, M.; Blinc, R. Spontaneous Flexoelectric/Flexomagnetic Effect in Nanoferroics. *Phys. Rev. B* **2009**, *79*, 165433.
18. Sabirianov, R. F.; Lukashev, P. V. Magneto-Elastic Properties of Frustrated Triangular Magnetic Structure: Flexomagnetic Effect. 2010; http://meetings.aps.org/link/BAPS.2010.MAR.Q34.8.
19. Vaz, C. A. F. Electric Field Control of Magnetism in Multiferroic Heterostructures. *J. Phys.: Condens. Matter* **2012**, *24*, 333201.
20. Vaz, C. A. F.; Hoffman, J.; Segal, Y.; Reiner, J. W.; Grober, R. D.; Zhang, Z.; Ahn, C. H.; Walker, F. J. Origin of the Magnetoelectric Coupling Effect in Pb($Zr_{0.2}$ $Ti_{0.8}$)O_3/$La_{0.8}$ $Sr_{0.2}$ MnO_3 Multiferroic Heterostructures. *Phys. Rev. Lett.* **2010**, *104*, 127202.
21. Molegraaf, H. J. A.; Hoffman, J.; Vaz, C. A. F.; Gariglio, S.; van der Marel, D.; Ahn, C. H.; Triscone, J.-M. Magnetoelectric

Effects in Complex Oxides with Competing Ground States. *Adv. Mater.* **2009**, *21*, 3470–3474.
22. Vaz, C. A. F.; Segal, Y.; Hoffman, J.; Grober, R. D.; Walker, F. J.; Ahn, C. H. Temperature Dependence of the Magnetoelectric Effect in $Pb(Zr_{0.2}\ Ti_{0.8})O_3/La_{0.8}Sr_{0.2}MnO_3$ Multiferroic Heterostructures. *Appl. Phys. Lett.* **2010**, *97*, 042506.
23. Dörr, K.; Thiele, C. Multiferroic Bilayers of Manganites and Titanates. *Phys. Status Solidi B* **2006**, *243*, 21–28.
24. Hezareh, T.; Razavi, F. S.; Kremer, R. K.; Habermeier, H.-U.; Lebedev, O. I.; Kirilenko, D.; Tendeloo, G. V. Effect of $PbZr_{0.52}Ti_{0.48}O_3$ Thin Layer on Structure, Electronic and Magnetic Properties of $La_{0.65}Sr_{0.35}MnO_3$ and $La_{0.65}Ca_{0.30}MnO_3$ Thin-Films. *J. Appl. Phys.* **2011**, *109*, 113707.
25. Zheng, R.; Wang, Y.; Liu, Y.; Gao, G.; Fei, L.; Jiang, Y.; Chan, H.; Li, X.; Luo, H.; Li, X. Epitaxial Growth and Interface Strain Coupling Effects in Manganite Film/Piezoelectric-Crystal Multiferroic Heterostructures. *Mater. Chem. Phys.* **2012**, *133*, 42–46.
26. Vrejoiu, I.; Ziese, M.; Setzer, A.; Esquinazi, P. D.; Birajdar, B. I.; Lotnyk, A.; Alexe, M.; Hesse, D. Interfacial Strain Effects in Epitaxial Multiferroic Heterostructures of $PbZr_xTi_{1-x}O_3/La_{0.7}Sr_{0.3}MnO_3$ Grown by Pulsed-Laser Deposition. *Appl. Phys. Lett.* **2008**, *92*, 152506.
27. Shu, L.; Li, Z.; Ma, J.; Gao, Y.; Gu, L.; Shen, Y.; Lin, Y.; Nan, C. W. Thickness-Dependent Voltage-Modulated Magnetism in Multiferroic Heterostructures. *Appl. Phys. Lett.* **2012**, *100*, 022405.
28. Liu, M.; Li, S.; Obi, O.; Lou, J.; Rand, S.; Sun, N. X. Electric Field Modulation of Magnetoresistance in Multiferroic Heterostructures for Ultralow Power Electronics. *Appl. Phys. Lett.* **2011**, *98*, 222509.
29. Arredondo, M.; Ramasse, Q. M.; Weyland, M.; Mahjoub, R.; Vrejoiu, I.; Hesse, D.; Browning, N. D.; Alexe, M.; Munroe, P.; Nagarajan, V. Direct Evidence for Cation Non-Stoichiometry and Cottrell Atmospheres around Dislocation Cores in Functional Oxide Interfaces. *Adv. Mater.* **2010**, *22*, 2430–2434.
30. Arredondo, M.; Weyland, M.; Hambe, M.; Ramasse, Q. M.; Munroe, P.; Nagarajan, V. Chemistry of Ruddlesden-Popper Planar Faults at a Ferroelectric-Ferromagnet Perovskite Interface. *J. Appl. Phys.* **2011**, *109*, 084101.
31. Chakhalian, J.; Millis, A. J.; Rondinelli, J. Whither the Oxide Interface. *Nat. Mater.* **2012**, *11*, 92–94.
32. Wolf, S. A.; Lu, J.; Stan, M. R.; Chen, E.; Treger, D. M. The Promise of Nanomagnetics and Spintronics for Future Logic and Universal Memory. *Proc. IEEE* **2010**, *98*, 2155–2168.
33. Raveau, B.; Maignan, A.; Mahendiran, R.; Khomskii, D.; Martin, C.; Hébert, S.; Hervieu, M.; Frésard, R. Instability of Magnetism and Conductivity in CMR Manganites: Role of Mn-Site Doping and Thermal Cycling. *J. Phys. Chem. Solids* **2002**, *63*, 901–905.
34. Chen, J.; Lu, H.; Liu, H.-J.; Chu, Y.-H.; Dunn, S.; Ostrikov, K.; Gruverman, A.; Valanoor, N. Interface Control of Surface Photochemical Reactivity in Ultrathin Epitaxial Ferroelectric Films. *Appl. Phys. Lett.* **2013**, *102*, 182904.
35. Karthik, J.; Damodaran, A. R.; Martin, L. W. Epitaxial Ferroelectric Heterostructures Fabricated by Selective Area Epitaxy of $SrRuO_3$ Using an MgO Mask. *Adv. Mater.* **2012**, *24*, 1610–1615.
36. Yu, P.; Luo, W.; Yi, D.; Zhang, J. X.; Rossell, M. D.; Yang, C.-H.; You, L.; Singh-Bhalla, G.; Yang, S. Y.; He, Q.; *et al*. Interface Control of Bulk Ferroelectric Polarization. *Proc. Natl. Acad. Sci. U.S.A.* **2012**, *109*, 9710–9715.
37. Afanasjev, V. P.; Petrov, A. A.; Pronin, I. P.; Tarakanov, E. A.; Kaptelov, E. J.; Graul, J. Polarization and Self-Polarization in Thin $PbZr_{1-x}Ti_xO_3$ (PZT) Films. *J. Phys.: Condens. Matter* **2001**, *13*, 8755–8763.
38. Jia, C.-L.; Nagarajan, V.; He, J.-Q.; Houben, L.; Zhao, T.; Ramesh, R.; Urban, K.; Waser, R. Unit-Cell Scale Mapping of Ferroelectricity and Tetragonality in Epitaxial Ultrathin Ferroelectric Films. *Nat. Mater.* **2007**, *6*, 64–69.
39. Gao, P.; Nelson, C. T.; Jokisaari, J. R.; Baek, S.-H.; Bark, C. W.; Zhang, Y.; Wang, E.; Schlom, D. G.; Eom, C.-B.; Pan, X. Revealing the Role of Defects in Ferroelectric Switching with Atomic Resolution. *Nat. Commun.* **2011**, *2*, 591.
40. Lu, H.; George, T. A.; Wang, Y.; Ketsman, I.; Burton, J. D.; Bark, C.-W.; Ryu, S.; Kim, D. J.; Wang, J.; Binek, C.; *et al*. Electric Modulation of Magnetization at the $BaTiO_3/La_{0.67}Sr_{0.33}MnO_3$ Interfaces. *Appl. Phys. Lett.* **2012**, *100*, 232904.
41. Chen, H.; Ismail-Beigi, S. Ferroelectric Control of Magnetization in $La_{1-x}Sr_xMnO_3$ Manganites: A First-Principles Study. *Phys. Rev. B* **2012**, *86*, 1–13.
42. Freeland, J. W.; Kavich, J. J.; Gray, K. E.; Ozyuzer, L.; Zheng, H.; Mitchell, J. F.; Warusawithana, M. P.; Ryan, P.; Zhai, X.; Kodama, R. H.; *et al*. Suppressed Magnetization at the Surfaces and Interfaces of Ferromagnetic Metallic Manganites. *J. Phys.: Condens. Matter* **2007**, *19*, 315210.
43. Adamo, C.; Ke, X.; Wang, H. Q.; Xin, H. L.; Heeg, T.; Hawley, M. E.; Zander, W.; Schubert, J.; Schiffer, P.; Muller, D. A.; *et al*. Effect of Biaxial Strain on the Electrical and Magnetic Properties of (001) $La_{0.7}Sr_{0.3}MnO_3$ Thin Films. *Appl. Phys. Lett.* **2009**, *95*, 112504.
44. Angeloni, M.; Balestrino, G.; Boggio, N. G.; Medaglia, P. G.; Orgiani, P.; Tebano, A. Suppression of the Metal-Insulator Transition Temperature in Thin $La_{0.7}Sr_{0.3}MnO_3$ Films. *J. Appl. Phys.* **2004**, *96*, 6387.
45. Tsui, F.; Smoak, M. C.; Nath, T. K.; Eom, C. B. Strain-Dependent Magnetic Phase Diagram of Epitaxial $La_{0.67}Sr_{0.33}MnO_3$ Thin Films. *Appl. Phys. Lett.* **2000**, *76*, 2421.
46. Ranno, L.; Llobet, A.; Tiron, R.; Favre-Nicolin, E. Strain-Induced Magnetic Anisotropy in Epitaxial Manganite Films. *Appl. Surf. Sci.* **2002**, *188*, 170–175.
47. Millis, A. J.; Darling, T.; Migliori, A. Quantifying Strain Dependence in "Colossal" Magnetoresistance Manganites. *J. Appl. Phys.* **1998**, *83*, 1588.
48. Cao, J.; Wu, J. Strain Effects in Low-Dimensional Transition Metal Oxides. *Mater. Sci. Eng., R* **2011**, *71*, 35–52.
49. Kanki, T.; Tanaka, H.; Kawai, T. Anomalous Strain Effect in $La_{0.8}Ba_{0.2}MnO_3$ Epitaxial Thin Film: Role of the Orbital Degree of Freedom in Stabilizing Ferromagnetism. *Phys. Rev. B* **2001**, *64*, 224418.
50. Hytch, M.; Snoeck, E.; Kilaas, R. Quantitative Measurement of Displacement and Strain Fields From HREM Micrographs. *Ultramicroscopy* **1998**, *74*, 131–146.
51. Hytch, M.; Houdellier, F. Mapping Stress and Strain in Nanostructures by High-Resolution Transmission Electron Microscopy. *Microelectron. Eng.* **2007**, *84*, 460–463.
52. Yang, F.; Kemik, N.; Biegalski, M. D.; Christen, H. M.; Arenholz, E.; Takamura, Y. Strain Engineering to Control the Magnetic and Magnetotransport Properties of $La_{0.67}Sr_{0.33}MnO_3$ Thin Films. *Appl. Phys. Lett.* **2010**, *97*, 092503.
53. Zubko, P.; Catalan, G.; Buckley, A.; Welche, P.; Scott, J. Strain-Gradient-Induced Polarization in $SrTiO_3$ Single Crystals. *Phys. Rev. Lett.* **2007**, *99*, 167601.
54. Eliseev, E. A.; Glinchuk, M. D.; Khist, V.; Skorokhod, V. V.; Blinc, R.; Morozovska, A. N. Linear Magnetoelectric Coupling and Ferroelectricity Induced by the Flexomagnetic Effect in Ferroics. *Phys. Rev. B* **2011**, *84*, 174112.
55. Zubko, P.; Catalan, G.; Tagantsev, A. K. Flexoelectric Effect in Solids. *Annu. Rev. Mater. Res.* **2013**, *43*, 387–421.
56. Park, S.; Lee, Y.; Prokhorov, V. Effects of Lattice-Strain-Induced Distortion and Jahn-Teller Coupling in $La_{0.8}Sr_{0.2}MnO_3/La_{0.8}Ca_{0.2}MnO_3$ Epitaxial Films. *J. Korean Phys. Soc.* **2004**, *45*, 47–50.
57. Kübler, J.; William, A.; Sommers, C. Formation and Coupling of Magnetic Moments in Heusler Alloys. *Phys. Rev. B* **1983**, *28*, 1745–1755.
58. Lampis, N.; Franchini, C.; Satta, G.; Geddo-Lehmann, A.; Massidda, S. Electronic Structure of $PbFe_{1/2}Ta_{1/2}O_3$: Crystallographic Ordering and Magnetic Properties. *Phys. Rev. B* **2004**, *69*, 064412.
59. Cammarata, A.; Rondinelli, J. M. Octahedral Engineering of Orbital Polarizations in Charge Transfer Oxides. *Phys. Rev. B* **2013**, *87*, 155135.
60. Maurice, J.-L. L.; Pailloux, F.; Barthélémy, A.; Durand, O.; Imhoff, D.; Lyonnet, R.; Rocher, A.; Contour, J.-P. P.; Barthelemy, A. Strain Relaxation in the Epitaxy of $La_{2/3}Sr_{1/3}MnO_3$ Grown by Pulsed-Laser Deposition on $SrTiO_3$(001). *Philos. Mag.* **2003**, *83*, 3201–3224.

61. Dey, P.; Nath, T. K.; Taraphder, A. Effect of Substrate-Induced Strain on Transport and Magnetic Properties of Epitaxial $La_{0.67}Sr_{0.33}MnO_3$ Thin Films. *Appl. Phys. Lett.* **2007**, *91*, 012511.
62. Haghiri-Gosnet, A.-M. A.; Renard, J.-P. CMR Manganites: Physics, Thin Films and Devices. *J. Phys. D: Appl. Phys.: Appl. Phys.* **2003**, *36*, R127–R150.
63. Pesquera, D.; Herranz, G.; Barla, A.; Pellegrin, E.; Bondino, F.; Magnano, E.; Sánchez, F.; Fontcuberta, J. Surface Symmetry-Breaking and Strain Effects on Orbital Occupancy in Transition Metal Perovskite Epitaxial Films. *Nat. Commun.* **2012**, *3*, 1189.
64. Varela, M.; Lupini, A.; Benthem, K. V.; Borisevich, A.; Chisholm, M.; Shibata, N.; Abe, E.; Pennycook, S. Materials Characterization in the Aberration-Corrected Scanning Transmission Electron Microscope. *Annu. Rev. Mater. Res.* **2005**, *35*, 539–569.
65. Varela, M.; Oxley, M.; Luo, W.; Tao, J.; Watanabe, M.; Lupini, A.; Pantelides, S.; Pennycook, S. Atomic-Resolution Imaging of Oxidation States in Manganites. *Phys. Rev. B* **2009**, *79*, 085117.
66. Loomer, D. B.; Al, T. A.; Weaver, L.; Cogswell, S. Manganese Valence Imaging in Mn Minerals at the Nanoscale Using STEM-EELS. *Am. Mineral.* **2007**, *92*, 72–79.
67. Shah, A.; Zhai, X.; Jiang, B.; Wen, J.-G.; Eckstein, J.; Zuo, J.-M. Electron Energy-Loss Study of the Electronic Structure of Atomic Scale $SrTiO_3$-$SrMnO_3$-$LaMnO_3$ Superlattices. *Phys. Rev. B* **2008**, *77*, 2–7.
68. Shah, A. B.; Ramasse, Q. M.; Zhai, X.; Wen, J. G.; May, S. J.; Petrov, I.; Bhattacharya, A.; Abbamonte, P.; Eckstein, J. N.; Zuo, J.-M. Probing Interfacial Electronic Structures in Atomic Layer $LaMnO_3$ and $SrTiO_3$ Superlattices. *Adv. Mater.* **2010**, *22*, 1156–1160.
69. Shah, A.; Ramasse, Q.; May, S.; Kavich, J.; Wen, J.; Zhai, X.; Eckstein, J.; Freeland, J.; Bhattacharya, A.; Zuo, J. Presence and Spatial Distribution of Interfacial Electronic States in $LaMnO_3$-$SrMnO_3$ Superlattices. *Phys. Rev. B* **2010**, *82*, 1–10.
70. Schmid, H. K.; Mader, W. Oxidation States of Mn and Fe in Various Compound Oxide Systems. *Micron* **2006**, *37*, 426–432.
71. Samet, L.; Imhoff, D.; Maurice, J.-L.; Contour, J.-P.; Gloter, A.; Manoubi, T.; Fert, A.; Colliex, C. EELS Study of Interfaces in Magnetoresistive LSMO/STO/LSMO Tunnel Junctions. *Eur. Phys. J. B* **2003**, *34*, 179–192.
72. Hong, X.; Posadas, A.; Ahn, C. H. Examining the Screening Limit of Field Effect Devices *via* the Metal-Insulator Transition. *Appl. Phys. Lett.* **2005**, *86*, 142501.
73. Dzero, M.; P, G. L.; Kresin, V. Z.; Gor'Kov, L. P. On Magnetoconductivity of Metallic Manganite Phases and Heterostructures. *Int. J. Mod. Phys. B* **2003**, *17*, 2095–2115.
74. Ahn, C. H.; Di Ventra, M.; Eckstein, J. N.; Frisbie, C. D.; Gershenson, M. E.; Goldman, A. M.; Inoue, I. H.; Mannhart, J.; Millis, A. J.; Morpurgo, A. F.; *et al*. Electrostatic Modification of Novel Materials. *Rev. Mod. Phys.* **2006**, *78*, 1185–1212.
75. Krivanek, O. L.; Corbin, G. J.; Dellby, N.; Elston, B. F.; Keyse, R. J.; Murfitt, M. F.; Own, C. S.; Szilagyi, Z. S.; Woodruff, J. W. An Electron Microscope for the Aberration-Corrected Era. *Ultramicroscopy* **2008**, *108*, 179–95.
76. Mitchell, D. R. G.; Schaffer, B. Scripting-Customized Microscopy Tools for Digital Micrograph. *Ultramicroscopy* **2005**, *103*, 319–332.
77. Koch, C. Determination of Core Structure Periodicity and Point Defect Density Along Dislocations. Ph.D. thesis, Arizona State University, 2002.
78. Saito, M.; Kimoto, K.; Nagai, T.; Fukushima, S.; Akahoshi, D.; Kuwahara, H.; Matsui, Y.; Ishizuka, K. Local Crystal Structure Analysis with 10-pm Accuracy Using Scanning Transmission Electron Microscopy. *J. Electron Microsc.* **2009**, *58*, 131–136.
79. Johnson, C.; Bording, J.; Zhu, Y. Structural Inhomogeneity and Twinning in $YBa_2Cu_3O_{7-\delta}$ Superconductors: High-Resolution Transmission Electron Microscopy Measurements. *Phys. Rev. B* **2008**, *78*, 014517.
80. Dudarev, S. L.; Savrasov, S. Y.; Humphreys, C. J.; Sutton, A. P. Electron-Energy-Loss Spectra and the Structural Stability of Nickel Oxide: An LSDA+U Study. *Phys. Rev. B* **1998**, *57*, 1505–1509.
81. Rappe, A.; Rabe, K.; Kaxiras, E.; Joannopoulos, J. Optimized Pseudopotentials. *Phys. Rev. B* **1990**, *41*, 1227–1230.
82. Perdew, J. P.; Burke, K.; Ernzerhof, M. Generalized Gradient Approximation Made Simple. *Phys. Rev. Lett.* **1996**, *77*, 3865–3868.
83. Perdew, J.; Ruzsinszky, A.; Csonka, G.; Vydrov, O.; Scuseria, G.; Constantin, L.; Zhou, X.; Burke, K. Restoring the Density-Gradient Expansion for Exchange in Solids and Surfaces. *Phys. Rev. Lett.* **2008**, *100*, 136406.
84. Marzari, N.; Vanderbilt, D.; De Vita, A.; Payne, M. Thermal Contraction and Disordering of the Al(110) Surface. *Phys. Rev. Lett.* **1999**, *82*, 3296–3299.
85. Monkhorst, H. J.; Pack, J. D. Special Points for Brillouin-Zone Integrations. *Phys. Rev. B* **1976**, *13*, 5188–5192.
86. Ma, C.; Yang, Z.; Picozzi, S. *Ab Initio* Electronic and Magnetic Structure in $La_{0.67}Sr_{0.33}MnO_3$: Strain and Correlation Effects. *J. Phys.: Condens. Matter* **2006**, *18*, 7717–7728.